## PAPER

Check for updates

# Enhanced visible transmittance and reduced transition temperature for VO₂ thin films modulated by index-tunable SiO₂ anti-reflection coatings

Maodong Zhu, [ID] [ab] Hongji Qi,*[a] Bin Wang,[a] Hu Wang,[a] Dongping Zhang*[c] and Weizhong Lv[d]

The low visible transmission is one of the bottleneck problems for the application of vanadium dioxide films since the high refractive index (RI) of VO₂ films results in strong reflection in the visible wavelength. To address this problem, in this paper, high-purity VO₂ films were deposited on fused silica by DC reactive magnetron sputtering at low temperature of 320 °C. Silica sol–gel coatings with tunable refractive index (RI) coated onto VO₂ films have been fabricated to enhance visible transmittance with the potential application in the field of smart windows. SiO₂ coatings with tunable RI (1.16–1.42 at $\lambda = 700$ nm) were prepared by sol–gel dip-coating technique. The double structure SiO₂/VO₂ films were characterized through several techniques, including X-ray diffraction, UV-VIS-NIR spectrophotometry and scanning electron microscopy. Compared with the single-layer VO₂ film ($\Delta T_{sol}$ of 6.25% and $T_{lum}$ of 38.58%), the three kinds of SiO₂/VO₂ bilayer films had higher $T_{lum}$ (41.93–50.44%) and larger $\Delta T_{sol}$ (8.15–8.51%) simultaneously due to significantly decreased reflectance. Moreover, the crystallization properties of VO₂ films are essentially unchanged by applying a SiO₂ top layer, while the phase transition temperature and thermal hysteresis width of sample S116 are lower than those of pure VO₂ film. The presented RI-tunable SiO₂ coatings, can regulate optical properties continuously for various VO₂ substrates, paving the way for practical applications of VO₂ films in the field of smart windows or others.

## 1. Introduction

Vanadium dioxide (VO₂) is the best thermochromic material for energy-efficient smart windows.[1,2] At the critical temperature (∼68 °C), a reversible semiconductor-to-metal transition occurs in bulk VO₂.[3] Accompanied with the crystal structure transitioning from rutile phase (R) to monoclinic phase (M), VO₂ exhibits a drastic change in electrical conductivity and NIR optical transmittance.[4] Such specific features make VO₂ a potential candidate in the application of thermochromic energy-efficient smart windows, uncooled infrared (IR) microbolometers, laser protection and optical storage devices.[5–8] High-purity VO₂ films can be fabricated by many preparation methods, including the pulsed laser deposition, sol–gel method, chemical vapor deposition (CVD), thermal evaporation, atomic layer deposition and magnetron sputtering.[9–14] Among these, magnetron sputtering technology shows great advantages for the application of VO₂ films in smart windows due to the good uniformity and potential for industrialization.[15]

Up till now, there has been no successful application of vanadium dioxide in the field of smart windows. To realize an available solution, several challenges needed to be overcame: low solar modulating ability, unattractive color, high transition temperature and especially low visible transmittance. Generally, the low transmission of single 80 nm VO₂ film can only reach 40% in the visible region (380–780 nm).[16] There have been various popular methods to enhance the visible transmittance of VO₂ films: metal-ion doping,[17] multilayer structure,[18] porous texture,[19] etc. Moreover, VO₂ films with different nanostructures can behaver enhanced $T_{lum}$ and $\Delta T_{sol}$, such as moth eye structure,[20] photonic structure,[21] plasmonic structure[22] and grided structure[23]. Additionally, applying antireflection coatings (ARCs) on the film surface can also be a promising approach to improve the visible transmittance of VO₂ films through TiO₂, ZnO, ZrO₂ or SiO₂, etc.,[24] which is useful in industrial applications. The anti-reflective devise of double-layer films should be enhanced as the high RI and reflectivity of VO₂ films in the

[a]Key Laboratory of Materials for High Power Laser, Shanghai Institute of Optics and Fine Mechanics, Chinese Academy of Sciences, Shanghai, 201800, China. E-mail: qhj@siom.ac.cn

[b]University of Chinese Academy of Sciences, Beijing, 100049, China

[c]Shenzhen Key Laboratory of Advanced Thin Film and Applications, College of Physics and Energy, Shenzhen University, Shenzhen, 518060, China. E-mail: zdpsiom@szu.edu.cn

[d]Shenzhen University, Shenzhen, 518060, China

visible region. However, most of the overcoats are usually with high RI, expensive and energy-consuming. It is worth noting that compared with other antireflection coatings, the $SiO_2$ coatings with low RI prepared by low-cost sol–gel methods behaved some advantages of large-area, widespread used and anti-oxidation.[25,26] Much research has been devoted to the fabrication of $SiO_2/VO_2$ double-layer structure to improve the visible transmission of $VO_2$ films significantly. Yu et al. increased the $T_{lum}$ of $VO_2$ film from 37.6% to 47.7% via $SiO_2/VO_2$ composite structure, while $\Delta T_{sol}$ exhibited an obvious decrease trend from 8.06% to 7.62%.[27] Zhang et al. introduced $SiO_2$ with RI of 1.299 as an antireflection coating coated on the $VO_2$ film, which improved the visible transmission from 69.8% to 80.0% significantly, whereas the NIR control capability was also slightly decreased from 12.6% to 10.2%.[28]

Therefore, in this study, $SiO_2$ anti-reflection coatings with tunable refraction index were coated on $VO_2$ films to enhance $\Delta T_{sol}$ and $T_{lum}$ simultaneously and continuously. Furthermore, the RI tunability of top $SiO_2$ coatings can be applied to not only the $VO_2$ continuous thin films but also the nanocomposites and micro-patterned $VO_2$ films to improve the nano-thermochromism effect.[29] In addition, an anti-oxidation overcoat is also necessary for the unstable $VO_2$ films. Index-tunable anti-reflection $SiO_2$ coatings optimized by sol–gel method prepared on the surface of $VO_2$ films by sol–gel dip-coating technique. The effect of RI tunability of $SiO_2$ coatings on the thermochromism and optical properties of $VO_2$ films was investigated.

## 2. Experimental details

$VO_2$ films were deposited on the fused silica by reactive magnetron sputtering technique. The deposition chamber was pumped to a base pressure of $4 \times 10^{-4}$ Pa by using a turbo molecular pump, and pre-cleaned in Ar gases for 10 min to remove contamination from the target surface. The vanadium target ($\Phi$60 mm) of purity 99.999% was used and the power density of V target was 4.2 W $cm^{-2}$. The distance of target-substrate was approximately 100 mm. Pure oxygen gas and argon gas were introduced to chamber at 1.8 sccm and 40 sccm, respectively. The deposition pressure and substrate temperature were maintained at 0.5 Pa and 320 °C, respectively. The deposition time was 30 min and the thickness of $VO_2$ films was controlled accurately to 150 nm. A schematic of DC magnetron sputtering is shown in Fig. 1(a). For low refractive silica ($n = 1.16$), the $SiO_2$ sols were prepared by base catalysis of ammonia, mixed with the teraethoxysilane (TEOS), $H_2O$, $NH_3$ and ethanol ($C_2H_5OH$). The molar ratio of TEOS, $H_2O$, $C_2H_5OH$ and $NH_3$ was
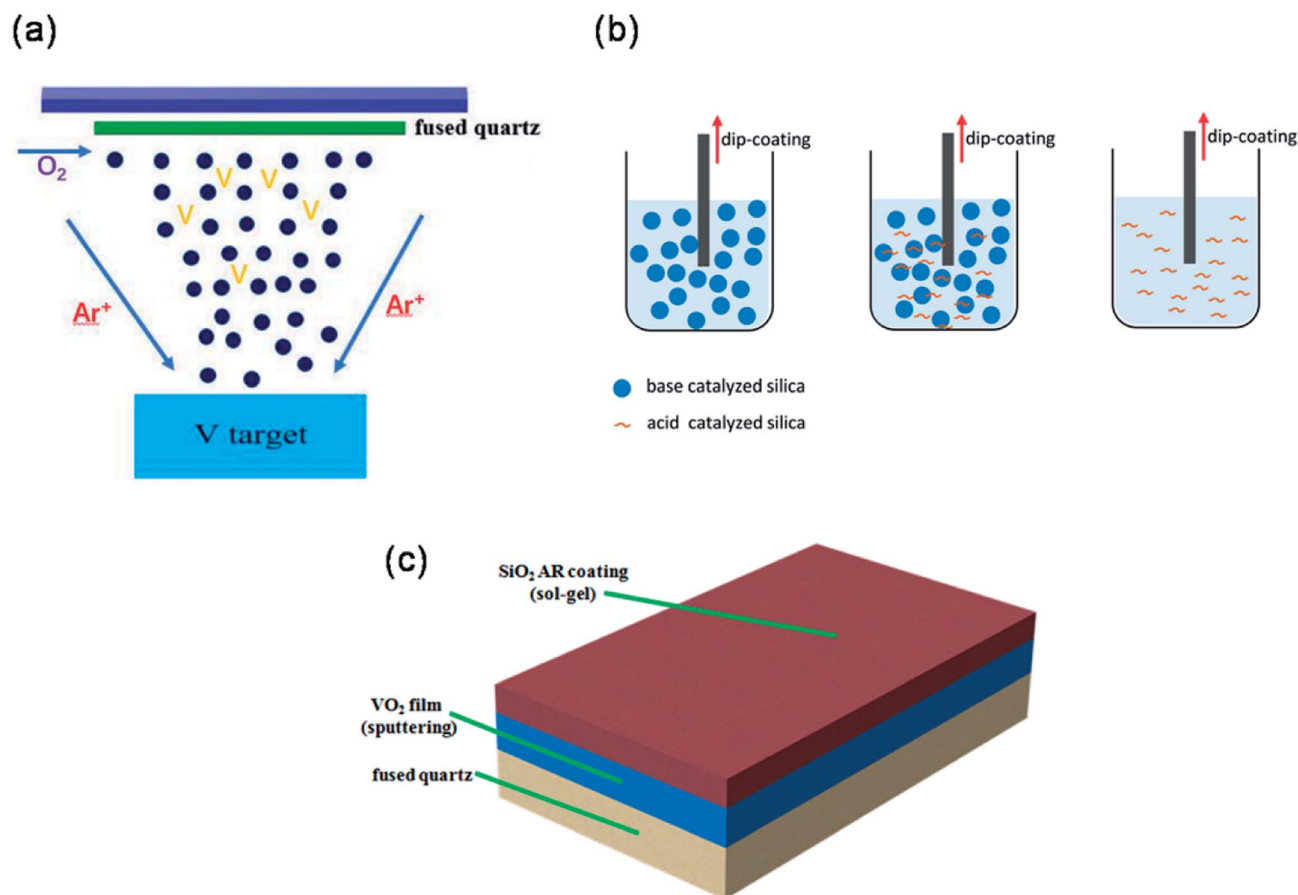


Fig. 1 Schematic diagrams of procedure of preparation of (a) $VO_2$ films and (b) $SiO_2$ sols. (c) Schematic illustration of the structure of $SiO_2/VO_2$ double-layer film.

$1 : 2 : 34.2 : 0.9$.[30] High refractive silica ($n = 1.42$) was synthesized by mixing teraethoxysilane (TEOS), $H_2O$, HCl and ethanol ($C_2H_5OH$). The molar ratio of TEOS, $H_2O$, $C_2H_5OH$ and HCl was $1 : 4 : 20 : 0.05$.[31] The $SiO_2$ coating with refractive index of 1.34 was prepared by mixing low refractive silica and high refractive silica with a molar ratio of 7 : 3.

The above resulting chemical reagents were stirred for 5 h and placed into an oven to age for 4 days. $VO_2$ films ($\Phi30$ mm, $d = 3$ mm) were coated with the three kinds of silicas by a dip coating process with a withdrawal speed of 7 cm min$^{-1}$, and then were baked at 180 °C for 24 h. The thickness of $SiO_2$ antireflection coating was about 110 nm. The schematics of preparation process of $SiO_2$ sols and dip coating process are shown Fig. 1(b). The $SiO_2/VO_2$ bilayer films coated by $SiO_2$ coatings with refractive indices of 1.16, 1.34 and 1.42 are denoted as S116, S134 and S142, respectively. And the $VO_2$ film without $SiO_2$ antireflection is marked as PVO$_2$. Fig. 1(c) illustrates the structure of $VO_2$ film on fused quartz with a $SiO_2$ antireflection coating. The optical transmittance of the $SiO_2/VO_2$ bilayer films were studied with a PerkinElmer Lambda 950 UV-VIS-NIR spectrophotometer from 250 to 2500 nm. A spectroscopic ellipsometer (Horiba uvisel 2) was used to characterize the refractive indices and physics thickness of $SiO_2$ coatings. The microstructure characterization of pure $VO_2$ and $SiO_2/VO_2$ bilayer films was measured by X-ray diffraction (Rigaku Ultima IV) with a $2\theta$ geometry. In addition, the optical transition behavior was studied by Thin film phase transition measurement system (PERFECT PTM1700) to collect the IR transmittance of films at a fixed wavelength (1550 nm) against temperature with an interval of 1.0 °C. The surface morphologies of the films were observed using a field-emission scanning electron microscope (Zeiss Supra 5S). The calculation of integral visible transmittance ($T_{lum}$, 380–780 nm) and solar transmittance ($T_{sol}$, 250–2500 nm) can refer to our previous work.[16]

## 3. Results and discussion

The refractive index of $SiO_2$ films with wavelength were measured by using ellipsometry and fitted by Cauchy ellipsometry model. Fig. 2 shows the refractive indices of $SiO_2$ antireflection coatings dipped by base catalyzed silica, acid catalyzed silica and mixed of them on the fused quartz. The refractive index of the $SiO_2$ film prepared by base catalyzed silica was measured to be ~1.16 at 700 nm, considerably lower than that prepared by acid catalyzed silica (~1.42) or that prepared by mixed of base and acid catalyzed silica (~1.34). On the other hand, the wavelength dispersions of the refractive index and extinction coefficient of pure $VO_2$ films below and above phase transition temperature were also measured and fitted by ellipsometry, which can be found from our previous work.[5]

Fig. 3(a) shows the XRD patterns of both bottom-layer and double-layer thin films on quartz substrates, including the standard pattern of monoclinic (M) $VO_2$ (PDF#82-0661). All the diffraction peaks of bottom-layer and double-layer films are similar, which correspond with the characteristic pattern of the $VO_2$ M-phase. It is worth noting that no other impurity peaks (such as $V_2O_3$, $V_2O_5$ or $V_4O_9$) can be observed in the XRD
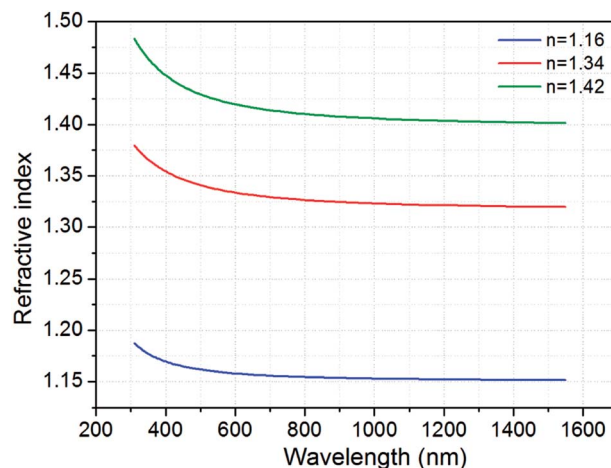


**Fig. 2** Dispersion curves of the refractive indices of the $SiO_2$ AR coatings prepared on the fused quartz.

patterns, indicating the formation of high-purity single crystal $VO_2$ films. These reveal that high-quality $VO_2$ films were obtained through DC reactive magnetron sputtering at low substrate temperature and the crystalline of $VO_2$ in double-layer film was unchanged after coated with sol–gel silica antireflection coatings. Additionally, the broad peaks in the range of 10° to 25° were assigned to fused quartz substrates. The fine patterns of $VO_2$ (011) peaks is shown in Fig. 3(b). It can be obvious seen that the values of two film samples are both slightly smaller than 27.827° of $VO_2$ powder diffraction, and the value of intense diffraction peak position of the double-layer $SiO_2/VO_2$ film sample is slightly smaller than 27.805° of the pure $VO_2$ film sample. The stress in films could be calculated by the formula:[15]

$$\sigma = \frac{E}{2v}\frac{d_0 - d}{d_0} \tag{1}$$

where $d$ and $d_0$ are the lattice distances in the strained and unstrained states, respectively. $E$ and $v$ are Young's modulus and Poisson's ratio of the film, respectively. The lattice coefficient could be obtained according to Bragg formula:

$$2d\sin\theta = k\lambda \tag{2}$$

where $\theta$ is the X-ray diffraction angle, and $\lambda$ is the X-ray wavelength. The compressive stress in double-layer $SiO_2/VO_2$ film sample is larger than that of pure $VO_2$ film after calculation from the above formulas.

Fig. 4 shows the top-view SEM images of pure $VO_2$ and $SiO_2/VO_2$ bilayer films. For the pure $VO_2$ film, rice-like nanoparticles scattered on the surface, indicating the good crystallinity of the sample. The morphology is porous for the sample S116, while the sample S142 behaved a denser structure without any pores on the surface. The surface morphology of sample S134 shows both characteristic mentioned above. Moreover, the cross-sectional SEM image of sample S116 is shown in the inset image of Fig. 4, in which an obvious interface between the 110 nm $SiO_2$ antireflective layer and 150 nm $VO_2$ film can be observed.
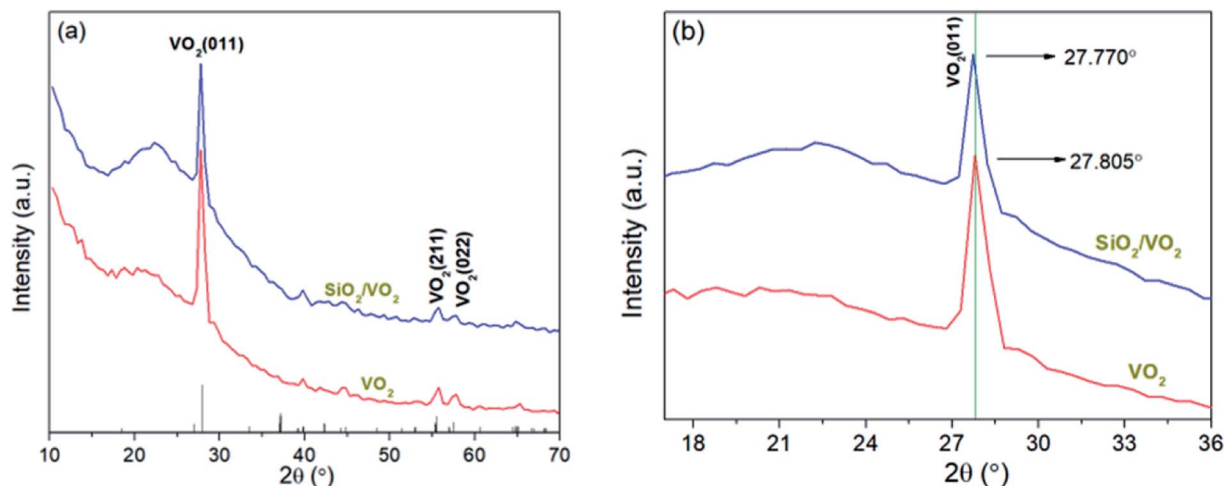
**Fig. 3** XRD spectra of the pure VO$_2$ film and SiO$_2$/VO$_2$ film: (a) normalized patterns; (b) fine patterns of VO$_2$ (011) peaks.

Fig. 5(a) shows the temperature-dependent transmittance of the pure VO$_2$ film and S116 bilayer film sample at $\lambda = 1550$ nm. Thermal hysteresis loop is evident for both film samples and the semiconductor-to-metal transition occurred, indicating that the double-layer SiO$_2$/VO$_2$ film sample maintained the phase transition properties. Compared with the pure VO$_2$ film, the enhancement of transmittance at $\lambda = 1550$ nm is obvious, and the highest value can reach 72% for the sample S116. The tunable-RI SiO$_2$ coatings can significantly suppress the optical reflection losses and improve light transmission.

Fig. 5(b) shows the Standard Gauss fitting derivative logarithmic plots, which were obtained by taking the derivative of the logarithmic transmittance with respect to the temperature of film sample. Phase transition temperature can be defined as $T_c = (T_l + T_h)/2$, and the thermal hysteresis width was calculated by $\Delta H = T_h - T_l$. The values of phase transition temperatures for pure VO$_2$ and S116 film sample are 63.5 °C and 60 °C, respectively, which are lower than 68 °C of the bulk VO$_2$. Moreover, the phase transition temperature of sample S116 is lower than that of pure VO$_2$ film. The main reason is that the larger compressive
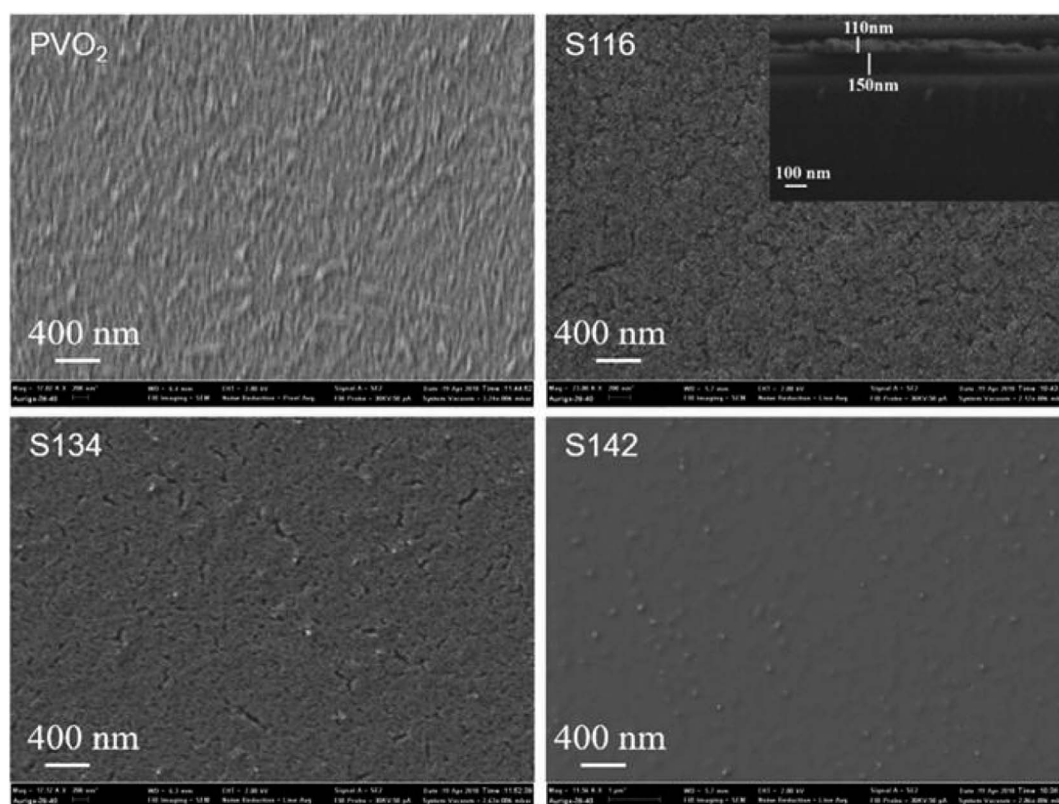


**Fig. 4** Top-view SEM images of pure VO$_2$ and SiO$_2$/VO$_2$ bilayer films.
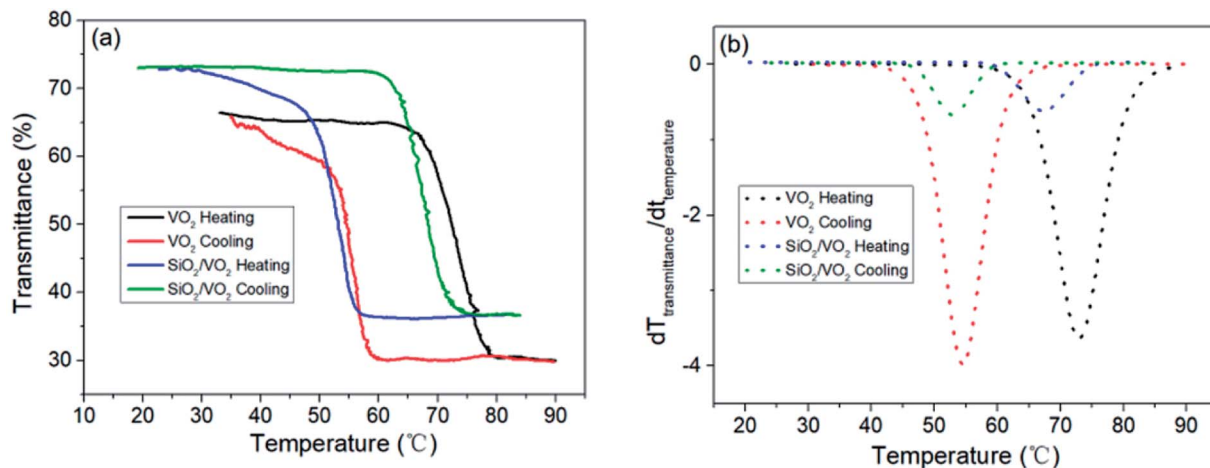
Fig. 5 (a) Transmittance hysteresis loops of pure $VO_2$ film and $SiO_2/VO_2$ bilayer films at $\lambda = 1550$ nm and (b) corresponding $dT/dt$ vs. temperature curve for film samples $PVO_2$ and S116.

stress existed in the double-layer film sample compared with the pure $VO_2$ film sample, which has been discussed in the XRD analysis. Our previous work[32] reported that the compressive stress changed the phase transition temperature of $VO_2$ film samples by applying $TiO_2$ buffer layers. The width of the hysteresis loop of sample S116 is 14.5 °C, which is also smaller than that of pure $VO_2$ film sample (18.5 °C). These results are different from other reports, which usually revealed that adding $SiO_2$ antireflection coatings would increase the $T_c$ and $\Delta H$ to a certain extent due to the existence of $SiO_2$ as thermal insulation.[24,28] The main reason of our experimental results may be the special porous morphology for the sample S116 with low refractive index.

To investigate the effect of RI-fixed $SiO_2$ coatings on the optical properties of the $VO_2$ films, the transmittance spectra were examined as shown in Fig. 6(a). The visible transmittance (at $\lambda = 700$ nm) and IR transmittance modulation (at $\lambda = 2500$ nm) of the film samples were calculated, as shown in Fig. 6(b). The transmittance at $\lambda = 700$ nm for the samples with $SiO_2$ antireflection coatings is higher than that of the single-layer $VO_2$ film, in which the sample with $SiO_2$ refractive index of

1.42 behaved the best. The visible transmittance at $\lambda = 700$ nm increased from 47% to 66% as the refractive index of $SiO_2$ antireflection coating increased from 1.16 to 1.42.

To fully display the superior optical properties of single-layer $VO_2$ and $SiO_2/VO_2$ double-layer films, the luminous transmittance ($T_{lum}$) and solar spectral transmittance ($T_{sol}$) of film samples were calculated based on the measured transmittance using the following eqn (3) and (4):

$$T_{sol} = \int \varphi_{sol}(\lambda)T(\lambda)d\lambda \Big/ \int \varphi_{sol}(\lambda)d\lambda \tag{3}$$

$$T_{lum} = \int \varphi_{lum}(\lambda)T(\lambda)d\lambda \Big/ \int \varphi_{lum}(\lambda)d\lambda \tag{4}$$

here, $T(\lambda)$ represents the transmittance, $\varphi_{sol}$ is the solar spectral irradiance for mass of 1.5. The angle between the sun and the horizon is above 37° and the wavelength is 280–2500 nm. $\varphi_{lum}$ is the standard luminous efficiency function of photonic vision and the wavelength for the $\varphi_{lum}$ is 380–780 nm. The values of $\Delta T_{sol}$ and $T_{lum(avg)}$ can be obtained as follows:
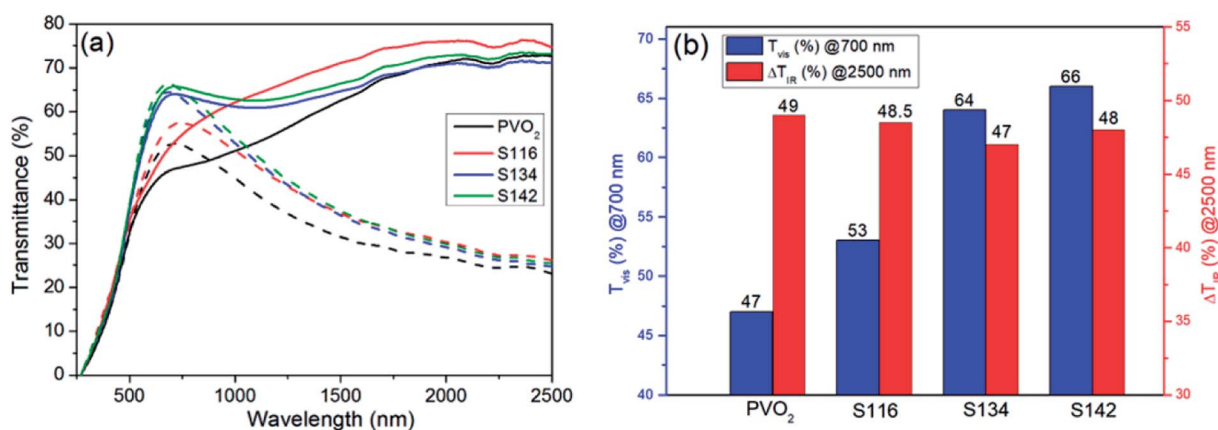


Fig. 6 (a) Transmittance spectra of pure $VO_2$ film and bilayer films. Solid lines represent the transmittance recorded at 25 °C and dotted lines measured at 80 °C. (b) $T_{vis}$ at $\lambda = 700$ nm and $\Delta T_{IR}$ at $\lambda = 2500$ nm for the samples.

**Table 1** Solar switching efficiency ($\Delta T_{sol}$) and luminous transmittance ($T_{lum}$) of the pure $VO_2$ film and $SiO_2/VO_2$ bilayer films compared with the reported studies

| Samples | $T_{sol,l}$ [%] | $T_{sol,h}$ [%] | $\Delta T_{sol}$ [%] | $T_{lum,l}$ [%] | $T_{lum,h}$ [%] | $T_{lum(avg)}$ [%] | $\Delta T_{lum}$ [%] |
|---|---|---|---|---|---|---|---|
| PVO$_2$ (this work) | 44.57 | 38.32 | 6.25 | 37.06 | 40.10 | 38.58 | 3.04 |
| S116 (this work) | 50.71 | 42.43 | 8.28 | 40.81 | 43.04 | 41.93 | 2.23 |
| S134 (this work) | 54.14 | 45.99 | 8.15 | 47.77 | 48.37 | 48.07 | 0.60 |
| **S142 (this work)** | **57.83** | **49.32** | **8.51** | **50.11** | **50.76** | **50.44** | **0.65** |
| VO$_2$@SiO$_2$ arrays[26] | — | — | 6.70 | — | — | 43.50 | — |
| SiO$_2$/VO$_2$ (ref. 27) | — | — | 7.62 | — | — | 47.70 | — |
| α-SiO$_2$/VO$_2$/α-SiO$_2$ (ref. 33) | 36.50 | 32.00 | 4.50 | 35.20 | 34.80 | 35.00 | 0.40 |
| TiO$_2$/VO$_2$ (ref. 34) | 46.25 | 39.26 | 6.99 | 49.15 | 45.05 | 47.10 | 4.10 |
| TiO$_2$(R)/VO$_2$(M)/TiO$_2$(A)[35] | 33.80 | 23.60 | 10.20 | 30.10 | 27.80 | 28.95 | 2.30 |
| Moth-eye structure[20] | 52.10 | 45.00 | 7.10 | 43.60 | 45.30 | 44.50 | −1.70 |
| VO$_2$/SiO$_2$/TiO$_2$ coating[36] | 28.83 | 13.55 | 15.29 | 17.81 | 18.23 | 18.02 | −0.42 |

$$\Delta T_{sol} = T_{sol,l} - T_{sol,h} \qquad (5)$$

$$T_{lum(avg)} = (T_{lum,l} + T_{lum,h})/2 \qquad (6)$$

here, $T_{sol,l}$ indicates the solar transmittance in semiconductor state and $T_{sol,h}$ indicates the solar transmittance in metal state. $T_{lum,l}$ and $T_{lum,h}$ mean the luminous transmittance in the low temperature state and high temperature state, respectively.

The solar switching efficiency ($\Delta T_{sol}$) and visible transmittance ($T_{lum}$) of the pure $VO_2$ film and bilayer films are shown on Table 1. It is obvious that $T_{lum}$ and $\Delta T_{sol}$ of the $SiO_2/VO_2$ films were all higher than the pure $VO_2$ film. Furthermore, the $T_{lum,l}$ and $T_{lum,h}$ of these samples both increased obviously as the refractive indices of $SiO_2$ coatings increased from 1.16 to 1.42, and the values of $\Delta T_{sol}$ also exhibited a slightly increasing trend at the same time. The maximum values of $T_{lum}$ and $\Delta T_{sol}$ for film sample S142 can reach 50.44% and 8.51%, respectively. This result was better than the values of reported $VO_2$@SiO$_2$ arrays prepared by rapid thermal annealing of sputtered vanadium films,[26] $SiO_2/VO_2$ double-layered films obtained vis plasma enhanced chemical vapor deposition,[27] α-SiO$_2$/VO$_2$/α-SiO$_2$ multi-layered films and TiO$_2$/VO$_2$ films deposited by radio frequency reactive magnetron sputtering.[33,34] Although the TiO$_2$(R)/VO$_2$(M)/TiO$_2$(A)[35] multi-layered films made through radio frequency reactive magnetron sputtering and VO$_2$/SiO$_2$/TiO$_2$ (ref. 36) films fabricated vis atmospheric-pressure chemical vapor deposition behaved higher $\Delta T_{sol}$ than our result, the values of their $T_{lum(avg)}$ were lower. More detailed results about recent studies were summarized in Table 1. In this work, the formation of smoother and denser film surface after $SiO_2$ coating can decrease the light scattering of the sample and enhance the visible transmittance. These results indicate that applying $SiO_2$ antireflection coatings with tunable refraction index can be an efficient way to enhance the visible transmittance of $VO_2$ films simultaneously and continuously.

## 4. Conclusion

In this work, $SiO_2/VO_2$ bilayer films were synthesized successfully by magnetron sputtering and sol–gel method. The crystallization properties of $VO_2$ films is essentially unchanged by applying $SiO_2$ top layer. The bilayer films can behave high transmittance and good thermochromic performance when compared with the single-layer pure $VO_2$ film. For the sample S142, the maximum value of $T_{lum}$ can reach 50.44%. For the sample S116, the width of hysteresis loop and transition temperature are 14.5 °C and 60 °C, respectively, which are smaller than those of pure $VO_2$ film sample (18.5 °C and 63.5 °C). Moreover, the $T_{lum}$ of these bilayer films increased obviously as the refractive index of $SiO_2$ antireflective layer increased from 1.16 to 1.42, and the $\Delta T_{sol}$ exhibited a slightly increasing trend. Hence, the enhancement of $T_{lum}$ and $\Delta T_{sol}$ simultaneously and continuously provides a meaningful solution for $VO_2$-based thermochromic energy-efficient smart windows.

## Conflicts of interest

There are no conflicts to declare.

## Acknowledgements

## References

1 Z. Y. Cao, Y. Lu, X. D. Xiao, Y. J. Zhan, H. L. Cheng and G. Xu, *Mater. Lett.*, 2017, **209**, 609–612.

2 J. B. Kana Kana, G. Vignaud, A. Gibaud and M. Maaza, *Opt. Mater.*, 2016, **54**, 165–169.

3 L. L. Fan, X. Q. Wang, F. Wang, Q. F. Zhang, L. Zhu, Q. Q. Meng, B. l. Wang, Z. M. Zhang and C. W. Zou, *RSC Adv.*, 2018, **8**, 19151–19156.

4 H. Y. Xu, Y. H. Huang, S. Liu, K. W. Xu, F. Ma and P. K. Chu, *RSC Adv.*, 2016, **6**, 79383–79388.

5 D. P. Zhang, M. D. Zhu, Y. Liu, K. Yang, G. X. Liang, Z. H. H. Zheng and X. M. Cai, *J. Alloys Compd.*, 2016, **659**, 198–202.

6 S. Chen, L. Dai, J. J. Liu, Y. F. Gao, X. L. Liu, Z. Chen, J. D. Zhou, C. X. Cao, P. G. Han, H. J. Luo and M. Kanahira, *Phys. Chem. Chem. Phys.*, 2013, **15**, 17537.

7 S. H. Chen, H. Ma, X. J. Yi, T. Xiong, H. C. Wang and C. J. Ke, *Sens. Actuators, A*, 2004, **115**, 28–31.

8 G. V. Jorgenson and J. C. Lee, *Sol. Energy Mater.*, 1986, **14**, 205.

9 J. Wu, W. X. Huang, Q. W. Shi, J. H. Cai, D. Zhao, Y. B. Zhang and J. Z. Yan, *Appl. Surf. Sci.*, 2013, **268**, 556–560.

10 K. Martens, I. P. Radu, S. Mertens, X. Shi, L. Nyns, S. Cosemans, P. Favia, H. Bender, T. Conard, M. Schaekers, S. De Gendt, V. Afanas'ev, J. A. Kittl, M. Heyns and M. Jurczak, *J. Appl. Phys.*, 2012, **112**, 124501.

11 V. Thery, A. Boulle, A. Crunteanu, J. C. Orlianges, A. Beaumont, R. Mayet, A. Mennai, F. Cosset, A. Bessaudou and M. Fabert, *J. Appl. Phys.*, 2017, **121**, 055303.

12 D. Vernardou, D. Louloudakis, E. Spanakis, N. Katsarakis and E. Koudoumas, *Sol. Energy Mater. Sol. Cells*, 2014, **128**, 36–40.

13 J. Sakai, M. Zaghrioui, V. T. Phuoc, S. Roger, C. Autret-Lambert and K. Okimura, *J. Appl. Phys.*, 2013, **113**, 123503.

14 Y. Huang, D. P. Zhang, Y. Liu, J. C. Jin, Y. Yang, T. Chen, H. Guan, P. Fan and W. Z. Lv, *Appl. Surf. Sci.*, 2018, **456**, 545–551.

15 M. D. Zhu, H. J. Qi, C. Li, B. Wang, H. Wang, T. R. Guan and D. P. Zhang, *Appl. Surf. Sci.*, 2018, **453**, 23–30.

16 M. D. Zhu, H. J. Qi, B. Wang, H. Wang, T. R. Guan and D. P. Zhang, *J. Alloys Compd.*, 2018, **740**, 844–851.

17 J. D. Zhou, Y. F. Gao, X. L. Liu, Z. Chen, L. Dai, C. X. Cao, H. J. Luo, M. Kanahira, C. Sun and L. M. Yan, *Phys. Chem. Chem. Phys.*, 2013, **15**, 7505.

18 N. R. Mlyuka, G. A. Niklasson and C. G. Granqvist, *Sol. Energy Mater. Sol. Cells*, 2009, **93**, 1685–1687.

19 L. T. Kang, Y. F. Gao, H. J. Luo, Z. Chen, J. Du and Z. T. Zhang, *ACS Appl. Mater. Interfaces*, 2011, **3**, 135–138.

20 X. K. Qian, N. Wang, Y. F. Li, J. H. Zhang, Z. C. Xu and Y. Long, *Langmuir*, 2014, **30**, 10766–10771.

21 Y. Ke, I. Balin, N. Wang, Q. Lu, A. I. Y. Tok, T. J. White, S. Magdassi, I. Abdulhalim and Y. Long, *ACS Appl. Mater. Interfaces*, 2016, **8**, 33112–33120.

22 Y. J. Ke, X. L. Wen, D. Y. Zhao, R. C. Che, Q. H. Xiong and Y. Long, *ACS Nano*, 2017, **11**, 7542–7551.

23 C. Liu, Y. Long, S. Magdassi and D. Mandler, *Nanoscale*, 2017, **9**, 485.

24 C. Wang, L. Zhao, Z. Liang, B. Dong, L. Wan and S. Wang, *Sci. Technol. Adv. Mater.*, 2017, **18**, 563–573.

25 D. Li, Y. Shan, F. Huang and S. Ding, *Appl. Surf. Sci.*, 2014, **317**, 160–166.

26 L. W. Zhou, J. R. Liang, M. Hu, P. Li, X. L. Song, Y. R. Zhao and X. Y. Qiang, *Appl. Phys. Lett.*, 2017, **110**, 193901.

27 J. H. Yu, S. H. Nam, J. W. Lee and J. H. Boo, *Materials*, 2016, **9**, 556.

28 J. Zhang, J. Wang, C. M. Yang, H. B. Jia, X. M. Cui and S. C. Zhao, *Sol. Energy Mater. Sol. Cells*, 2017, **162**, 134–141.

29 C. Liu, S. C. Wang, Y. Zhou, H. B. Yang, Q. Lu, D. Mandler, S. Magdassi, C. Y. Tay and Y. Long, *J. Alloys Compd.*, 2018, **731**, 1197–1207.

30 B. Shen, H. Y. Li, H. Xiong, X. Zhang and Y. X. Tang, *Chin. Opt. Lett.*, 2016, **14**, 083101.

31 Q. Jia, *Acta Opt. Sin.*, 2004, **24**, 65.

32 D. P. Zhang, K. Yang, Y. Li, Y. Liu, M. D. Zhu, A. H. Zhong, X. M. Cai, P. Fan and W. Z. Lv, *J. Alloys Compd.*, 2016, **684**, 719–725.

33 H. Kakiuchida, P. Jin and M. Tazawa, *Sol. Energy Mater. Sol. Cells*, 2008, **92**, 1279–1284.

34 P. Jin, G. Xu, M. Tazawa and K. Yoshimura, *Jpn. J. Appl. Phys.*, 2002, **41**, L278–L280.

35 J. Zheng, S. Bao and P. Jin, *Nano Energy*, 2015, **11**, 136–145.

36 M. J. Powell, R. Quesada-Cabrera, A. Taylor, D. Teixeira, I. Papakonstantinou, R. G. Palgrave, G. Sankar and I. P. Parkin, *Chem. Mater.*, 2016, **28**, 1369–1376.